Scripta Materialia 235 (2023) 115599

Contents lists available at ScienceDirect

Scripta Materialia

journal homepage: www.journals.elsevier.com/scripta-materialia

Unraveling the superlattice effect for hexagonal transition metal diboride coatings

R. Hahn [a,*], A.A. Tymoszuk [a], T. Wojcik [a], E. Ntemou [b], O. Hunold [c], P. Polcik [d], S. Kolozsvári [d], D. Primetzhofer [b], P.H. Mayrhofer [e], H. Riedl [a,e]

[a] Christian Doppler Laboratory for Surface Engineering of High-Performance Components, TU Wien, Getreidemarkt 9, Vienna 1060, Austria
[b] Department of Physics and Astronomy, Uppsala University, Uppsala SE-75120, Sweden
[c] Oerlikon Balzers, Oerlikon Surface Solutions AG, Balzers 9496, Liechtenstein
[d] Plansee Composite Materials GmbH, Lechbruck am See D-86983, Germany
[e] Institute of Materials Science and Technology, TU Wien, Wien A-1060, Austria

ARTICLE INFO

Keywords:
Physical vapor deposition
Fracture toughness
Micromechanical testing
Diboride coatings
Superlattice

ABSTRACT

Superlattice structures enable the simultaneous enhancement in hardness (H) and fracture toughness (K_{IC}) of ceramic-like coatings. While a deeper understanding of this effect has been gained for fcc-structured transition metal nitrides (TMN), hardly any knowledge is available for hexagonal diborides (TMB_2). Here we show that superlattices can—similarly to nitrides—increase the hardness and toughness of diboride films. For this purpose, we deposited TiB_2/WB_2 and TiB_2/ZrB_2 superlattices with different bilayer periods (Λ) by non-reactive sputtering. Nanoindentation and in-situ microcantilever bending tests yield a distinct H peak for the TiB_2/WB_2 system (45.5 $\pm$ 1.3 GPa for $\Lambda = 6$ nm) but no increase in K_{IC} related to a difference in shear moduli (112 GPa). Contrary, the TiB_2/ZrB_2 system shows no peak in H, but for K_{IC} with 3.70 $\pm$ 0.26 MPa•$m^{1/2}$ at $\Lambda = 4$ nm originating from differences in lattice spacing (0.14 Å), hence causing coherent stresses retarding crack growth.

The fracture toughness of hard ceramic-like coatings can significantly be increased with a so-called superlattice (SL) structure, as recently discovered in the example of binary nitrides prepared by physical vapor deposition (PVD) [1–4]. Their characteristic parameter is the bilayer period Λ, which is the combined thickness of the two constituting layers [5]. The impact of a superlattice structure on hardness has been known for many years (especially for fcc nitrides), and one of the earlier works even shows twice the hardness for TiN/VN SLs with $\Lambda = 5.2$ nm compared to their monolithic counterparts [6]. This SL effect on hardness is regularly observed for nitrides with Λ between 5 and 10 nm [7] and essentially results from competing dislocation activity mechanisms, which are well explained in [8]. However, there is still a need to clarify the superlattice effect on fracture toughness since the measurement methodology excludes a significant contribution of dislocation movement [9]. In the present work, the concept of superlattice structures was applied to hexagonal transition metal diboride coatings and thoroughly investigated concerning their fracture toughness and hardness. To unravel the primary effect of a different lattice parameter or different shear moduli individually–being the suggested key factors for hardness and fracture toughness increase–we chose TiB_2/WB_2 with a high shear modulus difference combination ($\Delta G = 112$ GPa and $\Delta a = 0.01$ Å [10]) and TiB_2/ZrB_2 obtaining a significant difference in lattice parameters ($\Delta G = 27$ GPa and $\Delta a = 0.14$ Å [10]). Therefore, we prepared TiB_2/WB_2 and TiB_2/ZrB_2 multilayer coatings using an AJA International Orion 5 unbalanced magnetron sputtering system equipped with two 2″ (TiB_2 and WB_2) and one 3″ (ZrB_2) cathode. The ultrasonically cleaned single crystalline substrates (Si (100) and Al_2O_3 ($10\bar{1}1$)) were mounted on a rotating (1 s^{-1}) substrate holder and heated to the deposition temperature as well as Ar etched. The deposition was carried out at a total Ar pressure of 0.4 Pa using a computer-controlled shutter system to achieve the desired superlattice architecture. Details of the used deposition parameter and the final film thickness (determined using an FEI Quanta 250 FEGSEM) are presented in Table 1, the growth rates of our coatings were the following: 4.0 nm•min^{-1} for TiB_2, 29.4 nm•min^{-1} for ZrB_2, and 5.2 nm•min^{-1} for WB_2.

Fig. 1a shows a detailed view of the (001) peak for the TiB_2/WB_2 system. The structural data were recorded on Si (100) using a Panalytical XPert Pro-MPD θ-θ diffractometer in Bragg-Brentano

* Corresponding author.
E-mail address: rainer.hahn@tuwien.ac.at (R. Hahn).

https://doi.org/10.1016/j.scriptamat.2023.115599
Received 18 April 2023; Received in revised form 1 June 2023; Accepted 4 June 2023
Available online 8 June 2023

configuration equipped with a Cu K_α radiation source. All our thin films are stabilized in the so-called α structure (SG 191); notably, we do not observe any signs of the ω-modification (SG 194), which is suggested to be detrimental to coherent growth. The (001) orientation is predominant for the monolithic coatings and bilayer periods of 2, 4, and 6 nm, respectively. Higher bilayer periods tend to show a mixed (001) and (101) orientation (the (101) peak positions at $2\theta \sim 44°$ shown in Fig. S1). We observe an increase in satellite peaks visible with increasing bilayer periods. However, as soon as the (101) orientation becomes apparent, the number of satellite peaks decreases. Fig. 1b shows the corresponding (001) peak region of the TiB_2/ZrB_2 superlattices and monolithic coatings. Compared to the TiB_2/WB_2 system, the number of satellite peaks increases, and the (001) orientation is maintained. The dominant structure is exclusively α. Furthermore, the cumulative peak for the $\Lambda = 2$ nm coating shifts to higher 2θ values, mainly due to a higher Zr content (see Table 1). To confirm the bilayer period derived from dividing the total film thickness by the number of bilayers, we also calculated the values, as described in [11], see Table 1 and supplementary materials.

To further prove and thoroughly describe the morphology of the superlattice structure, selected samples have been investigated in the TEM. All TEM images were recorded using a Tecnai F20 operated at 200 kV and equipped with a FEG and a Gatan Rio camera. Fig. 2a shows an HR-TEM image of the 6 nm TiB_2/WB_2 sample, including an FFT of the entire image area, confirming the α structure. The bilayer period measured from this is 5.6 nm, fitting well with the SEM and XRD results. The dashed areas (marked with b, resp. c) show the sections used to generate an ABSF-filtered image [12], which was further investigated concerning the lattice spacing (Fig. 2d-f). We found that the lattice parameters of individual layers agreed with literature values: TiB_2 shows a lattice spacing d_{100} of 2.67 Å (2.63 Å according to PDF 00–035–0741 [13]), WB_2 of 2.72 Å (2.62 Å according to PDF 04–003–6624 [13]). This crystal direction is also where coherence stresses should occur, but this could not be verified based on the analysis. By the same methodology, we determined the c-axis parameters and verified a good agreement with the literature for TiB_2 with 3.25 Å; the literature value for d_{001} is 3.23 Å [13]. For WB_2, we measured a c-axis parameter of 3.19 Å, well within the limits given in [14], considering the highly defective growth during PVD.

A different situation is observed for the TiB_2/ZrB_2 sample with a 4 nm bilayer period. Here, we can also confirm the bilayer period measured by XRD and SEM in the TEM (3.76 nm) (Fig. 2g), but more considerable differences appear in the determined lattice parameters (Fig. 2h-l). While the d_{100} lattice parameter for the ZrB_2 single layer with 2.81 Å is close to the literature value (2.76 Å according to PDF

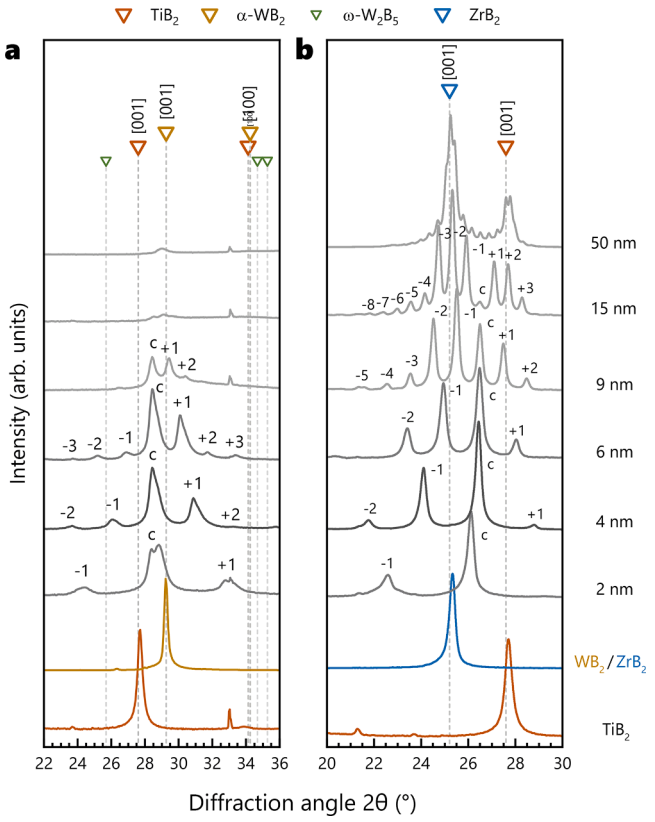

Fig. 1. X-ray diffraction patterns of (a) the (001) regions of TiB2/WB2 and (b) the (001) regions of TiB2/ZrB2. The bilayer period and the monolithic system of the XRDs are on the right side, and the triangles on the top mark the reference positions for the respective material system. The resulting cumulative peaks – due to overlapping contributions from the constituting layers, especially for small bilayer periods – are marked with "c," and the satellite peaks stemming from the layered structure are marked with "+*n*" and "-n" for positive and negative satellites, respectively.

Table 1
The used deposition parameter (the applied target current Ic, bias voltage Ub, and heater temperature Tc) for multilayer architectures and monolithic coatings, as well as the nominal bilayer period Λnom, the final experimental film thicknesses tf, and the experimental bilayer periods ΛSEM and ΛXRD. All three targets used had a purity of at least 99.5 at.% and have been manufactured by Plansee Composite Materials GmbH. For the growth of all films, a base pressure below 2•10−6 mbar was maintained. An etching procedure was applied for 10 min by introducing 20 sccm Argon, regulating the pressure to 6 Pa at a bias voltage of −750 V. The resulting bilayer period diverging from the nominal was calculated by dividing the film thickness by the number of bilayers. The TM/(TM+Ti) ratios were determined using an EDAX Octane Elite EDS detector using an FEI Quanta 200 SEM for Zr/(Zr+Ti) and measured by TOF-ERDA (see [24] and references therein) for W/(W+Ti), similar to the method described in [25]. The ERDA results show a B/Ti ratio of 2.66 and a W/B ratio of 2.00 for the monolithic coatings.

Coating	Λ_{nom} (nm)	I_c (A)	U_b (V)	T_c (°C)	t_f (μm)	Λ_{SEM} (nm)	Λ_{XRD} (nm)	TM/(TM+Ti))* (-)
TiB_2	–	0.6	−40	300	2.02	–	–	–
ZrB_2	–	0.75	−40	300	2.00	–	–	–
WB_2	–	0.3	−60	500	1.77	–	–	–
TiB_2/ZrB_2	2	0.6 and 0.75	−40	300	1.95	1.9	2.8	0.61
	4				1.87	3.7	3.9	0.48
	6				1.94	5.8	5.9	0.45
	9				1.98	8.9	9.2	0.47
	15				1.99	14.9	15.4	0.45
	50				1.99	49.7	–	0.47
TiB_2/WB_2	2	0.6 and 0.3	−60	500	2.11	2.1	2.1	0.54
	4				1.83	3.6	3.8	0.54
	6				1.82	5.5	5.6	0.55
	9				2.01	9.0	9.5	0.54
	15				2.03	15.2	–	0.56
	50				1.87	46.8	–	0.56

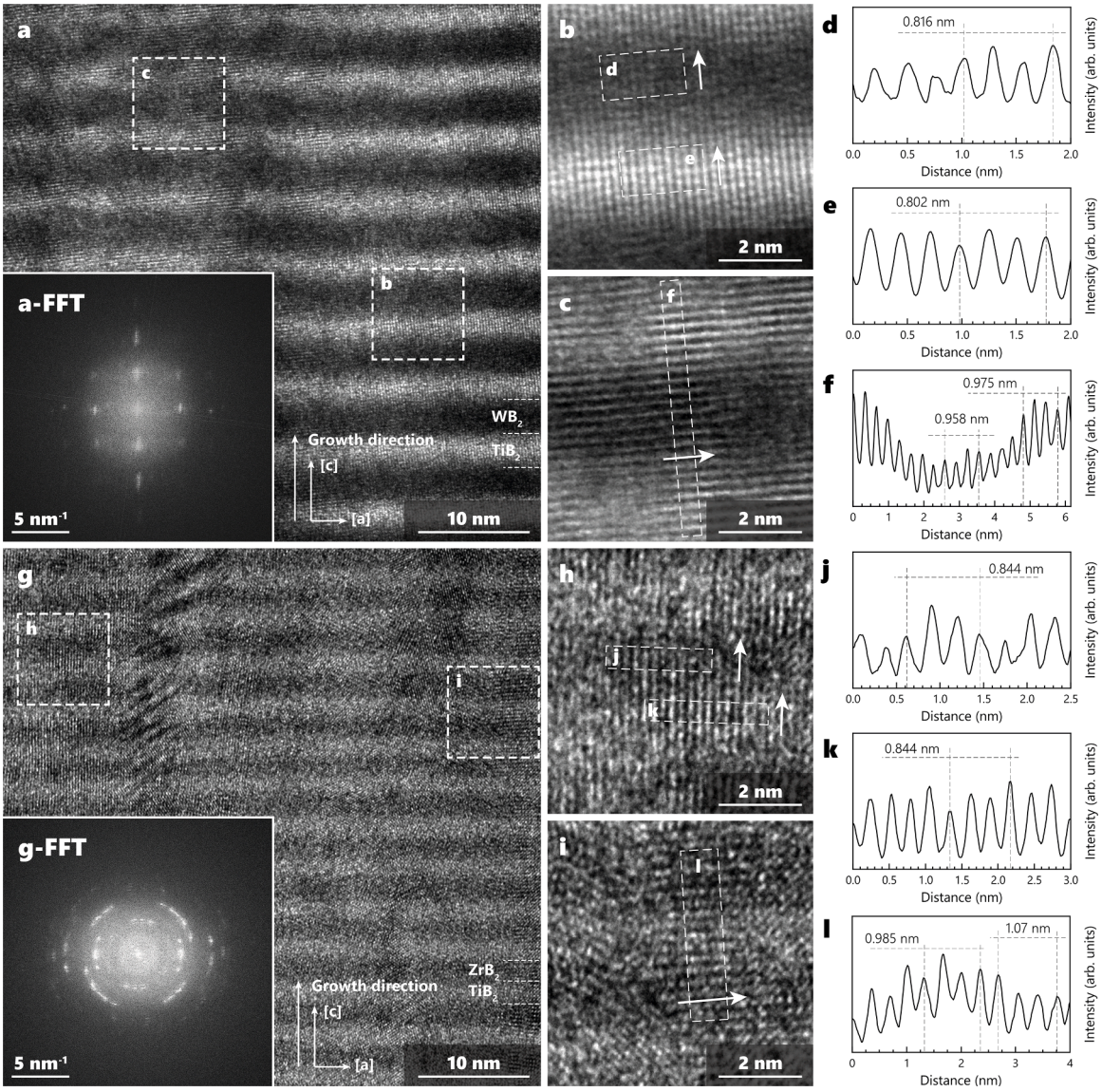

Fig. 2. High-resolution TEM images of the TiB_2/WB_2 sample with $\Lambda = 6$ nm and the TiB_2/ZrB_2 sample with $\Lambda = 4$ nm; the samples were prepared by applying a standard lift-out procedure using a ThermoFischer Scios 2 Dual Beam FIB. (a) shows an HR bright field image of a representative region of the TiB_2/WB_2 sample, including an FFT image of the whole area as well as the areas for further detailed analysis (marked with b and c). Panels (b) and (c) show ABSF-filtered images, including the areas that were used to determine lattice spacings (marked with d, e, and f). The arrows thereby show the direction in which the intensity was summed and afterward plotted in (d), (e), and (f). The same procedure was applied to our TiB_2/ZrB_2 sample: (g) shows the HR TEM image, including an FFT of the whole area, (h) and (i) a detailed view of the marked areas in (g), including marks for the intensity plots (j), (k), and (l). We measured 3 lattice distances for all intensity plots to obtain a more accurate average value for d_{100} and d_{001}.

00–034–0423 [13]), the TiB_2 single layer with the same measured lattice parameter is already clearly under the influence of coherence stress (2.81 Å measured instead of 2.63 Å). A difference can also be seen in the d_{001} values. Here, ZrB_2 was measured with 3.57 Å, and TiB_2 with 3.28 Å (the respective literature values are 3.53 Å, and 3.23 Å [13]). In summary, for the analysis of the lattice parameters, it can be said that, as theoretically predicted, the TiB_2/WB_2 system shows hardly any differences from the literature values, while the TiB_2/ZrB_2 system shows significant deviations from literature values in the d_{100} lattice parameter. Hence, coherency stresses should be present and influence the fracture properties of the latter system.

Fig. 3 presents Young's moduli and hardness of both systems and the respective monolithic coatings. These mechanical parameters were measured using a UMIS nanoindentation system equipped with a diamond Berkovich tip. For the Young's moduli in Fig. 3a, we observe that the measured values of the superlattice coatings tend to show lower values than the average ones of their individual components, with a bilayer period depending relation, peaking at 4 and 6 nm for TiB_2/ZrB_2 and TiB_2/WB_2, respectively.

Fig. 3b shows the hardness values of the TiB_2/WB_2 system for both substrates, sapphire and silicon. We observe an apparent bilayer period-dependent behavior due to the difference in shear moduli ($\Delta G = 112$ GPa) of TiB_2 and WB_2. The hardness peaks around 6 nm and is slightly higher than the average of its constituents. It is also worth mentioning that the constituents do not possess any significant difference in lattice parameters perpendicular to the growth direction. Hence, their difference in shear modulus mainly accompanies the enhancement. Fig. 3c shows the hardness vs. bilayer period progression for the second system, TiB_2/ZrB_2, which does not significantly differ in their elastic constants (253 and 226 GPa for TiB_2 and ZrB_2, respectively [10]). Importantly, we do not measure any bilayer period-dependent behavior in this case. The hardness values of the multilayers are at a level similar to the average of

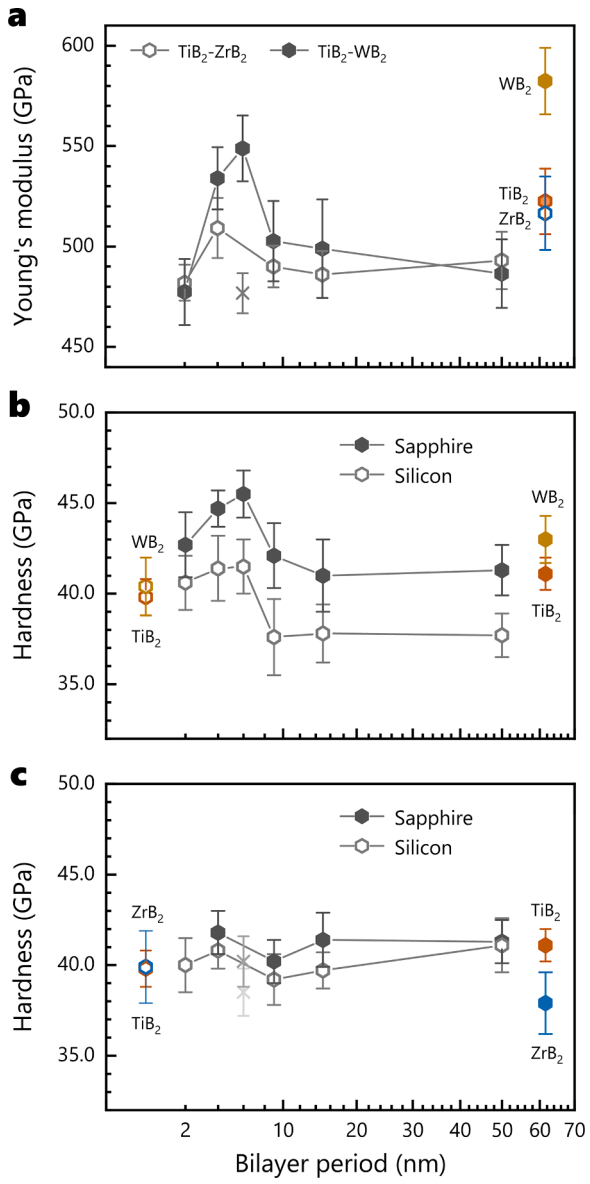

Fig. 3. (a) shows the Young's modulus of our coatings, hardness values for TiB_2/WB_2, and TiB_2/ZrB_2 (on Si and Sapphire substrates) are presented in (b) and (c), respectively. To achieve specific statistics, we performed 31 measurements for each sample with varying maximum loads from 3 to 45 mN, thereby ruling out measurements with indentation depths larger than 1/10th of the coating thickness. The hardness was calculated according to Oliver and Pharr [26], whereas Young's Modulus was determined according to [27] for the two different substrate types.

their components. It is also interesting that coherency stresses alone (although large) do not guarantee any significant hardness increase. Hence, concluding this figure, we see a typical behavior for the hardness progression for diboride-based superlattices dominated by the shear modulus (112 GPa, TiB_2/WB_2) difference, while the lattice parameters have a minor influence as described in [8].

Micro-cantilever bending tests have been conducted to prove the main influencing factors on fracture toughness. Therefore, the same SEM system used for the film thickness determination was equipped with a FemtoTools FT-NMT04 nanomechanical testing system for fracture toughness evaluation. FIB-milled cantilevers (ThermoFisher Scientific Scios2) were loaded in the growth direction with a wedge-shaped diamond tip until fracture (also in the growth direction). The cantilever dimensions were chosen to fulfill the criteria given by Brinckmann et al. [15,16]. In this case, the typical dimension of the cantilever was ~ 14 × 2 × 2 μm^3 with an average initial crack length of ~ 400 nm. We performed at least four successful experiments for each material system and architecture to calculate the fracture toughness according to Matoy et al. [17]. After testing and calculating the fracture toughness, we ensured that our values represented K_{IC} values by estimating the plastic zone size and comparing it to the critical dimensions [9].

Fig. 4a summarizes the results of our microcantilever bending tests. We observe a bilayer period-depending behavior for TiB_2/ZrB_2 superlattices, with a peak in fracture toughness at $K_{IC} = 3.7 \pm 0.26$ MPa•$m^{1/2}$ for $\Lambda = 6$ nm, clearly above the monolithic systems. This increase in K_{IC} has also been observed with other superlattice systems [2,3,18]. In contrast, the TiB_2/WB_2 system behaves differently: we do not observe a dependence of the fracture toughness on the bilayer period. In contrast, the measured K_{IC} values tend to decrease with decreasing Λ, although not significantly. The highest value of 3.0 ± 0.24 MPa•$m^{1/2}$ was achieved at a bilayer period of 50 nm, comparable to the constituents.

In the case of macroscopically residual stress-free material

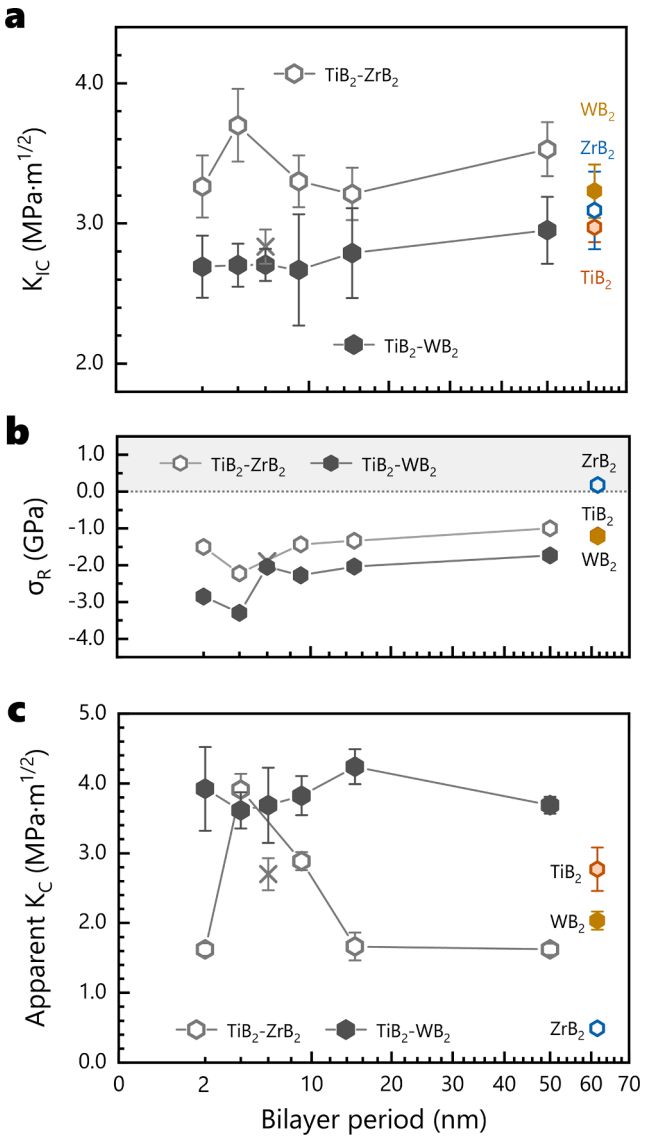

Fig. 4. (a) shows the intrinsic fracture toughness of our coatings. The residual stresses and indentation toughness on Si (100) are presented in (b) and (c), respectively. For the apparent fracture toughness K_C, an indentation process serving crack initiation and propagation was repeated four times over four series of measurements, with the applied force gradually increasing from 100 mN for the first series to 400 mN for the last.

properties, these results highlight coherency stresses' crucial role in increasing fracture toughness. While the TiB_2/ZrB_2 system (lattice mismatch of 0.14 Å) shows a pronounced peak in K_{IC}, this behavior is absent in the TiB_2/WB_2 system (difference in shear modulus 112 GPa). For comparison, the lattice parameters (in (100) direction) of the three material systems differ significantly for TiB_2 and ZrB_2 with 3.03 and 3.17 Å, respectively, whereas TiB_2 and WB_2 (3.020 Å) show almost no differences.

Relying on the findings obtained by [4], the lattice parameter difference of $\Delta a = 0.14$ Å existing between TiB_2 and ZrB_2 leads to the formation of coherent stresses, compressive in the ZrB_2 layers and tensile in the TiB_2 layers. The distortion energy of the ZrB_2 lattice associated with the compressive stresses impedes the progressive growth of a previously initiated crack, with the effectiveness of the energetic resistance increasing with the layer thickness. The maximum K_{IC} value was obtained for a bilayer period of $\Lambda = 4$ nm. With a progressive increase in layer thicknesses, the formation of interfacial misfit dislocations appears to be more energetically favorable for TiB_2 and ZrB_2 than their elastic lattice strain, resulting in the reduction of coherent stresses. Consequently, the distortion energy to be overcome by a crack in the ZrB_2 layer reduces, which decreases the intrinsic fracture toughness.

Fig. 4b shows the results of residual stress measurements (performed using a profilometer: Nanovea PS50) on Si substrates for TiB_2/WB_2 and TiB_2/ZrB_2 multilayer systems. Compressive residual stress states are predominant in all systems except the monolithic ZrB_2 layer. The residual stresses of the superlattice coatings show a slight dependence on the layer period for both variants. We observe an increase in the residual compressive stresses with decreasing layer period, in agreement with literature observations [19].

To further verify the observed findings, indentation fracture (IF) analysis took place in the same IBIS nanoindenter system described above, although a cube-corner diamond indenter tip was used to determine the fracture toughness – see Fig. 4c. For each radial crack that appeared at the corner of a pyramidal plastic indentation, the length c_{fra} was measured in the FEI Quanta 200 FEGSEM. In a further step, the associated K_c value was calculated using [20]. A penetration depth of the indenter tip smaller than ten percent of the layer thickness could not be observed; therefore, an influence of the substrate material on the fracture toughness had to be assumed. To reduce the effect of the violated condition on the K_C value, the approach according to [21] was suitable.

Using the IF method, there is an initially dramatic increase in fracture toughness for the TiB_2/ZrB_2 system from 1.62 ± 0.09 MPa$\sqrt{m}$ for $\Lambda = 2$ nm to the maximum value of 3.91 ± 0.23 MPa$\sqrt{m}$ for $= 4$ nm, followed by an equally significant decrease in the characteristic curve to $K_C = 1.66 \pm 0.2$ MPa$\sqrt{m}$, which subsequently takes a flat course leading to 1.62 ± 0.08 MPa$\sqrt{m}$ for a bilayer period of 50 nm. Apart from the increase in intrinsic fracture toughness between $\Lambda = 15$ and 50 nm, the K_C and K_{IC} values of the TiB_2/ZrB_2 system proceed in a congruent manner, as indicated by their high variance in a range from $\Lambda = 2$ to 15 nm and an explicit maximum for a layer period of 4 nm. Moreover, the characteristic values of those TiB_2/ZrB_2 layers grown with $\Lambda = 4$ and 9 nm turn out to be higher than the K_C and K_{IC} values of the respective tougher monolithic diboride layer.

The TiB_2/WB_2 system results in an initial decrease from $K_C = 3.92 \pm 0.6$ MPa$\sqrt{m}$ for $\Lambda = 2$ nm to $K_C = 3.61 \pm 0.26$ MPa$\sqrt{m}$ for $\Lambda = 4$ nm and a subsequent maximization to $K_C = 4.24 \pm 0.25$ MPa$\sqrt{m}$, with a final reduction to $K_C = 3.69 \pm 0.12$ MPa$\sqrt{m}$ for a layer period of 50 nm. Although the residual stresses and the K_C values of the TiB_2/WB_2 layers do not show a consistent trend, their higher compressive residual stresses, considered globally, offer a comprehensible justification for exceeding the K_C value exhibited by their constituents.

Because the K_C and K_{IC} evolution in the single-digit bilayer period hardly deviates, the main question, whether the shear moduli differences of two-layer materials dominate the superlattice effect on fracture toughness, can be negated for these hexagonal diborides.

Within this study, the enhancement of mechanical properties such as hardness and fracture toughness by superlattice structures could be successfully proven for physical vapor deposited hexagonal diborides. We could isolate the lattice parameter difference as the primary mechanism for increased toughness. At the layer interfaces, coherency stresses impede crack propagation due to the lattice mismatch ($\Delta a \sim 4.6\%$), demonstrated for TiB_2/ZrB_2 (i.e., K_C improvement by 30%). In contrast, a difference in shear modulus results in a distinct hardness peak attributed to hindered dislocation motion across the interface and within a single layer, as shown for TiB_2/WB_2. Nevertheless, the anisotropic properties (predominant [001] texture [14,22]) of hexagonal diborides, combined with the shear modulus differences, need to be considered to interpret the hardness evolution in the case of the TiB_2/WB_2 system. Additionally, for the TiB_2/ZrB_2 system, the influence of a possible tissue phase at the absolute values of the fracture toughness—not their progression as the elemental composition is similar throughout the coating series [23].

Declaration of Competing Interest

The authors declare that they have no known competing financial interests or personal relationships that could have appeared to influence the work reported in this paper.

Acknowledgments

The authors acknowledge TU Wien Bibliothek for financial support through its Open Access Funding Program. The financial support by the Austrian Federal Ministry for Digital and Economic Affairs, the National Foundation for Research, Technology and Development, and the Christian Doppler Research Association is gratefully acknowledged (Christian DopplerLaboratory "Surface Engineering of high-performanceComponents"). We also thank for the financial support of Plansee SE, Plansee Composite Materials GmbH, and Oerlikon Balzers, OerlikonSurface Solutions AG. In addition, we want to thank the X-ray center (XRC) of TU Wien for beam time and the electron microscopy center - USTEM TU Wien - for providing the SEM facilities. Accelerator operation at Uppsala University has been supported by the Swedish research council VR-RFI under grant agreement #2019–00191.

Supplementary materials

Supplementary material associated with this article can be found, in the online version, at doi:10.1016/j.scriptamat.2023.115599.

References

[1] J. Buchinger, N. Koutná, Z. Chen, Z. Zhang, P.H. Mayrhofer, D. Holec, M. Bartosik, Toughness enhancement in TiN/WN superlattice thin films, Acta Mater. 172 (2019) 18–29, https://doi.org/10.1016/J.ACTAMAT.2019.04.028.
[2] R. Hahn, M. Bartosik, R. Soler, C. Kirchlechner, G. Dehm, P.H. Mayrhofer, Superlattice effect for enhanced fracture toughness of hard coatings, Scr. Mater. (2016) 124, https://doi.org/10.1016/j.scriptamat.2016.06.030.
[3] R. Hahn, N. Koutná, T. Wójcik, A. Davydok, S. Kolozsvári, C. Krywka, D. Holec, M. Bartosik, P.H. Mayrhofer, Mechanistic study of superlattice-enabled high toughness and hardness in MoN/TaN coatings, Commun. Mater. 11 (1) (2020) 1–11, https://doi.org/10.1038/s43246-020-00064-4, 2020.
[4] A. Wagner, D. Holec, P.H. Mayrhofer, M. Bartosik, Enhanced fracture toughness in ceramic superlattice thin films: on the role of coherency stresses and misfit dislocations, Mater. Des. 202 (2021), 109517, https://doi.org/10.1016/j.matdes.2021.109517.
[5] M. Stueber, H. Holleck, H. Leiste, K. Seemann, S. Ulrich, C. Ziebert, Concepts for the design of advanced nanoscale PVD multilayer protective thin films, J. Alloys Compd. 483 (2009) 321–333, https://doi.org/10.1016/j.jallcom.2008.08.133.
[6] U. Helmersson, S. Todorova, S.A. Barnett, J.E. Sundgren, L.C. Markert, J.E. Greene, Growth of single-crystal TiN/VN strained-layer superlattices with extremely high mechanical hardness, J. Appl. Phys. 62 (1987) 481–484, https://doi.org/10.1063/1.339770.
[7] W.D. Muenz, D.B. Lewis, P.E. Hovsepian, C. Schönjahn, A. Ehiasarian, I.J. Smith, Industrial scale manufactured superlattice hard PVD coatings, Surf. Eng. 17 (2001) 15–27, https://doi.org/10.1179/026708401101517557.
[8] X. Chu, S.A. Barnett, Model of superlattice yield stress and hardness enhancements, J. Appl. Phys. 77 (1995) 4403–4411, https://doi.org/10.1063/1.359467.

[9] R. Pippan, S. Wurster, D. Kiener, Fracture mechanics of micro samples: fundamental considerations, Mater. Des. 159 (2018) 252–267, https://doi.org/10.1016/j.matdes.2018.09.004.
[10] F. Ricci, W. Chen, U. Aydemir, G.J. Snyder, G.M. Rignanese, A. Jain, G. Hautier, Data descriptor: an ab initio electronic transport database for inorganic materials, Sci. Data. 4 (2017) 1–13, https://doi.org/10.1038/sdata.2017.85.
[11] P.C. Yashar, W.D. Sproul, Nanometer scale multilayered hard coatings, Vacuum 55 (1999) 179–190, https://doi.org/10.1016/S0042-207X(99)00148-7.
[12] R. Kilaas, Optimal and near-optimal filters in high-resolution electron microscopy, J. Microsc. 190 (1998) 45–51, https://doi.org/10.1046/j.1365-2818.1998.3070861.x.
[13] S. Gates-Rector, T. Blanton, The powder diffraction file: a quality materials characterization database, Powder Diffr. 34 (2019) 352–360, https://doi.org/10.1017/S0885715619000812.
[14] C. Fuger, R. Hahn, L. Zauner, T. Wojcik, M. Weiss, A. Limbeck, O. Hunold, P. Polcik, H. Riedl, Anisotropic super-hardness of hexagonal WB2±z thin films, Mater. Res. Lett. 10 (2022) 70–77, https://doi.org/10.1080/21663831.2021.2021308.
[15] S. Brinckmann, C. Kirchlechner, G. Dehm, Stress intensity factor dependence on anisotropy and geometry during micro-fracture experiments, Scr. Mater. 127 (2017) 76–78, https://doi.org/10.1016/j.scriptamat.2016.08.027.
[16] S. Brinckmann, K. Matoy, C. Kirchlechner, G. Dehm, On the influence of microcantilever pre-crack geometries on the apparent fracture toughness of brittle materials, Acta Mater. 136 (2017) 281–287, https://doi.org/10.1016/J.ACTAMAT.2017.07.014.
[17] K. Matoy, H. Schönherr, T. Detzel, T. Schöberl, R. Pippan, C. Motz, G. Dehm, A comparative micro-cantilever study of the mechanical behavior of silicon based passivation films, Thin Solid Films 518 (2009) 247–256, https://doi.org/10.1016/j.tsf.2009.07.143.
[18] R. Hahn, M. Bartosik, M. Arndt, P. Polcik, P.H. Mayrhofer, Annealing effect on the fracture toughness of CrN/TiN superlattices, Int. J. Refract. Met. Hard Mater. (2017), https://doi.org/10.1016/j.ijrmhm.2017.11.008.
[19] D.J. Li, M. Cao, X.Y. Deng, X. Sun, W.H. Chang, W.M. Lau, Multilayered coatings with alternate ZrN and TiAlN superlattices, Appl. Phys. Lett. 91 (2007), 251908, https://doi.org/10.1063/1.2826284.
[20] B.R. Lawn, A.G. Evans, Elastic/plastic indentation damage in ceramics: the median/radial crack system, J. Am. Ceram. Soc. 63 (1980) 574–581.
[21] B. Bakhit, D.L.J. Engberg, J. Lu, J. Rosen, H. Högberg, L. Hultman, I. Petrov, J. E. Greene, G. Greczynski, Strategy for simultaneously increasing both hardness and toughness in ZrB 2 -rich Zr 1−x Ta x B y thin films, J. Vac. Sci. Technol. A 37 (2019), 031506, https://doi.org/10.1116/1.5093170.
[22] C. Fuger, R. Hahn, A. Hirle, P. Kutrowatz, M. Weiss, A. Limbeck, O. Hunold, P. Polcik, H. Riedl, Revisiting the origins of super-hardness in TiB2+z thin films – impact of growth conditions and anisotropy, Surf. Coat. Technol. (2022) 446, https://doi.org/10.1016/j.surfcoat.2022.128806.
[23] C. Fuger, R. Hahn, A. Hirle, T. Wojcik, P. Kutrowatz, F. Bohrn, O. Hunold, P. Polcik, H. Riedl, Tissue phase affected fracture toughness of nano-columnar TiB2 + z thin films, Mater. Res. Lett. 11 (2023) 613–622, https://doi.org/10.1080/21663831.2023.2204120.
[24] P. Ström, D. Primetzhofer, Ion beam tools for nondestructive in-situ and in-operando composition analysis and modification of materials at the Tandem laboratory in Uppsala, J. Instrum. (2022) 17, https://doi.org/10.1088/1748-0221/17/04/P04011.
[25] C. Fuger, V. Moraes, R. Hahn, H. Bolvardi, P. Polcik, H. Riedl, P.H. Mayrhofer, Influence of Tantalum on phase stability and mechanical properties of WB_2, MRS Commun. (2019) 1–6, https://doi.org/10.1557/mrc.2019.5.
[26] W.C. Oliver, G.M. Pharr, An improved technique for determining hardness and elastic modulus using load and displacement sensing indentation experiments, J. Mater. Res. 7 (1992) 1564–1583, https://doi.org/10.1557/JMR.1992.1564.
[27] A.C. Fischer-Cripps, Critical review of analysis and interpretation of nanoindentation test data, Surf. Coat. Technol. 200 (2006) 4153–4165, https://doi.org/10.1016/j.surfcoat.2005.03.018.